ADVANCED FUNCTIONAL MATERIALS
www.afm-journal.de

Materials Views
www.MaterialsViews.com

Triboelectric Nanogenerator as an Active UV Photodetector

*Zong-Hong Lin, Gang Cheng, Ya Yang, Yu Sheng Zhou, Sangmin Lee, and Zhong Lin Wang**

Self-powered nanosensors and nanosystems have attracted significant attention in the past decades and have gradually become the most desirable and promising prototype for environmental protection/detection because no battery is needed to power the device. Therefore, in this paper a design is proposed for a self-powered photodetector based on triboelectric nanogenerator (TENG) configuration. 3D dendritic TiO_2 nanostructures are synthesized as the built-in UV photodetector as well as the contact material of the TENG. The cost-effective, robust, and easily fabricated TENG-based photodetector presents superior photoresponse characteristics, which include an excellent responsivity over 280 A W^{-1}, rapid rise time (18 ms) and decay time (31 ms), and a wide detection range of light intensity from 20 $\mu W\ cm^{-2}$ to 7 $mW\ cm^{-2}$. In the last part of the paper, a stand-alone and self-powered environmental sensing device is developed by applying poly(methyl methacrylate) (PMMA) substrates and springs to assemble the TENG-based photodetector. These results indicate that the new prototype sensing device based on the TENG configuration shows great potential as a self-powered photodetector.

1. Introduction

Self-powered nanosensors and nanosystems that can function without external power sources have recently been demonstrated as new approaches for pH,[1] temperature,[2] biomolecules,[3,4] toxic pollutants,[5,6] and light[7,8] sensing. By harvesting energy directly from the environment, these self-powered devices are advantageous in minimizing the size and avoiding the use of environmentally unfriendly materials in battery.[9–12] Since the first invention of triboelectric nanogenerator (TENG) in 2012,[13] it has been developed into a new energy technology. TENG has been applied to efficiently convert the mechanical vibration into electricity. The generated output can instantaneously drive 600 light-emitting diodes (LEDs)[14] and charge a lithium ion battery for powering a wireless sensor and a commercial cell phone.[15] The fundamental mechanism of the TENG is based on surface charge transfer, which is through the contact between two materials with different triboelectric polarity. The serial contact and separation of the material surfaces with opposite charges establishes a potential difference, which will drive the electrons flow through the external load. Since the capability of surface charge transfer depends on the physical and chemical properties of the surfaces, we have previously found that the material surface can be further functionalized for selective detection of metal ions and small molecules, such as mercury ions[16] and catechin molecules.[17] These results show that TENG is a promising candidate for the development of self-powered nanosensors.

UV photodetectors have been widely used in communications, biological and chemical analysis, environmental monitoring, remote control, memory storage, and optoelectronic circuits.[18–20] Some prototype self-powered UV photodetectors based on photoelectrochemical cell[21,22] and p–n junction[23,24] have been reported. Self-powered UV photodetectors based on photochemical cell showed impressive performances. But they normally need to use I^-/I_3^- redox couple as the electrolyte, which is not ideal for long-term operation. The I^-/I_3^- redox couple is highly corrosive, photoreactive, volatile, and will interact with common metallic components and sealing materials. Therefore, other prototype self-powered UV photodetectors based on p-n junction were developed. Those photodetectors have the advantages of low applied field, fast response time, and no oxygen dependency. However, the sensitivity (6 $mW\ cm^{-2}$) could become a concern when detecting UV light with lower intensity, which is critical for environmental monitoring and medical therapy treatment.

In this paper, we demonstrate a fully integrated photodetector for UV light sensing based on TENG conformation. 3D dendritic TiO_2 nanostructures synthesized using a chemical bath deposition method were served as not only the built-in photodetector and but also as one of the contact materials of the TENG. By utilizing poly(methyl methacrylate) (PMMA) and spring to assemble the TENG-based photodetector, a stand-alone and self-powered environmental sensing device is developed. Through a periodic impact on the TENG by a linear motor or biomechanical movement (finger tapping),

Dr. Z.-H. Lin, Dr. G. Cheng, Dr. Y. Yang, Y. S. Zhou, Dr. S. Lee, Prof. Z. L. Wang
School of Material Science and Engineering
Georgia Institute of Technology
Atlanta, GA, 30332–0245, USA
E-mail: zlwang@gatech.edu
Prof. Z. L. Wang
Beijing Institute of Nanoenergy and Nanosystems
Chinese Academy of Sciences
Beijing, 100083, China
Dr. G. Cheng
Key Lab for Special Functional Materials
Henan University
Kaifeng, 475004, China

DOI: 10.1002/adfm.201302838

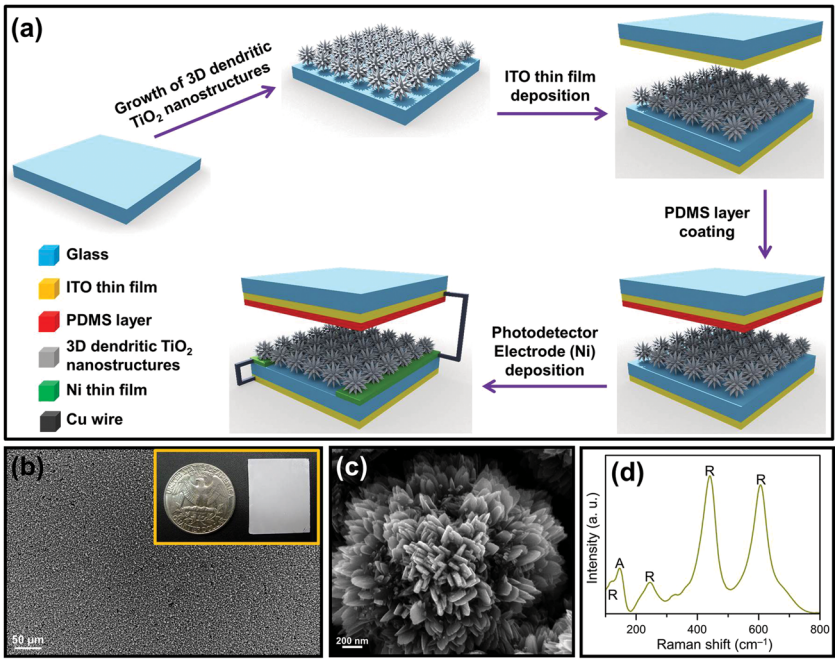

Figure 1. (a) Fabrication process of the self-powered UV photodetector. (b,c) SEM images and (d) Raman spectrum of the 3D dendritic TiO_2 nanostructures coated glass substrate.

a fast 18 ms rise and a 31 ms decay time, a high responsivity reaching 280 A W^{-1}, and a wide linear detection range starting from 20 μW cm^{-2} to 7 mW cm^{-2} were obtained.

2. Results and Discussion

The fabrication process of the active UV photodetector was detailed in **Figure 1**a. The demonstrated device is constituted by a layered structure of two plates. On the lower side, the TiO_2 plate is prepared. Firstly, 3D dendritic TiO_2 nanostructures were designed to grow directly onto a glass substrate through a facile, scalable, and low cost chemical bath deposition method. Glass was chosen as the substrate due to its high transparency, strength, low cost and light weight. During the growth of TiO_2 crystal, Ti(III) species were gradually oxidized to Ti(IV) species by dissolved O_2 and then hydrolyzed to form TiO_2.[25] Controlling the oxidation and hydrolysis of the Ti(III) precursor ($TiCl_3$) is the key factor to obtain TiO_2 nanomaterials with different morphologies.[26] Unlike the previous approach, we prepared the 3D dendritic TiO_2 nanostructures instead of single layer of vertically aligned TiO_2 nanoplatelet arrays by increasing the reaction time and growth cycles. Figure 1b displays the scanning electron microscope (SEM) image and photograph of 3D dendritic TiO_2 nanostructures coated glass, which can be easily observed with naked eyes that the nanostructures are uniformly distributed on the substrate. The enlarged SEM image (Figure 1c) further reveals the nanostructures are dendrite-like particles with an average size of 2 μm and composed by nanoplatelets with an average width of 28 nm and length of 160 nm, respectively. The crystal phase of the as-prepared 3D dendritic TiO_2 nanostructures is identified by Raman spectroscopy (Figure 1d). The strong Raman bands appearing at 131, 243, 440, and 606 cm^{-1} can be ascribed to the B_{1g}, two-phonon scattering, E_g, and A_{1g} modes of rutile phase, indicating the structure is mainly constructed by rutile TiO_2 nanoplatelets.[27] The XRD pattern shown in Figure S1 further validates the Raman result. The 3D nanostructures fabricated in this study are of great interest not only unique in the structural characteristics, but also remarkable in the electrical, chemical and optical properties.[28–30] Then a colorless thin film of indium tin oxide (ITO) was deposited on the back of the 3D dendritic TiO_2 nanostructures coated glass substrate as the conducting electrode. On the other plate, another ITO thin film is deposited between a glass substrate and a layer of polydimethylsiloxane (PDMS). PDMS is purposely chosen here for its advantages of high transparency, easy processing, and flat surface. Finally, the Ni thin film was selected to deposit as the electrodes of the built-in photodetector to ensure the Schottky contact can be created. The photodetector with Schottky contact has been proved to have the advantages of low dark current, high responsivity, and direct compatibility with modern high-speed integrated circuitry.[31,32] The built-in photodetector is then connected with the TENG to construct the active UV photodetector. The built-in photodetector in the device can function as a photoresistor. The resistance of the built-in photodetector varies upon UV light irradiation with different intensities, which will consequently affect the capability of the surface charge transfer during triboelectrification process and the output of the TENG. Therefore, the light intensity can be determined by monitoring the output of the TENG.

In order to clarify the stability of the active UV photodetector, we firstly measured the photoresponse switching behavior of the built-in photodetector. As shown in **Figure 2**a, the current signal can be reproducibly switched from the "On" state to the "Off" state by periodically turning the UV light (70 μW cm^{-2}) on and off at a bias of 5 V. From the enlarged single cycle of the photocurrent response displayed in Figure 2b, the rise time and decay time (t_r and t_d, defined as time to 1/e of the maximum photocurrent) of the photodetector achieved around 18 and 31 ms, which revealing the rapid photoresponse characteristics. Figure 2c shows the current–voltage (*I*–*V*) curves of the built-in photodetector under UV light irradiation with different intensities and in dark. Schottky barrier-like behavior of the built-in photodetector is observed from the *I*–*V* curve under dark condition (Figure S2a). In order to make a clear contrast between photocurrent and dark current, the *I*–*V* curves are plotted in a semi-log scale. Upon UV light irradiation, the current increases linearly with the applied voltage, indicating the change of Schottky contact to Ohmic contact between Ni electrodes and the built-in photodetector (Figure S2b). The photocurrent increases with the light intensity, consistent with the fact that the charge carrier photogeneration efficiency is proportional to the absorbed photon flux. The photocurrent

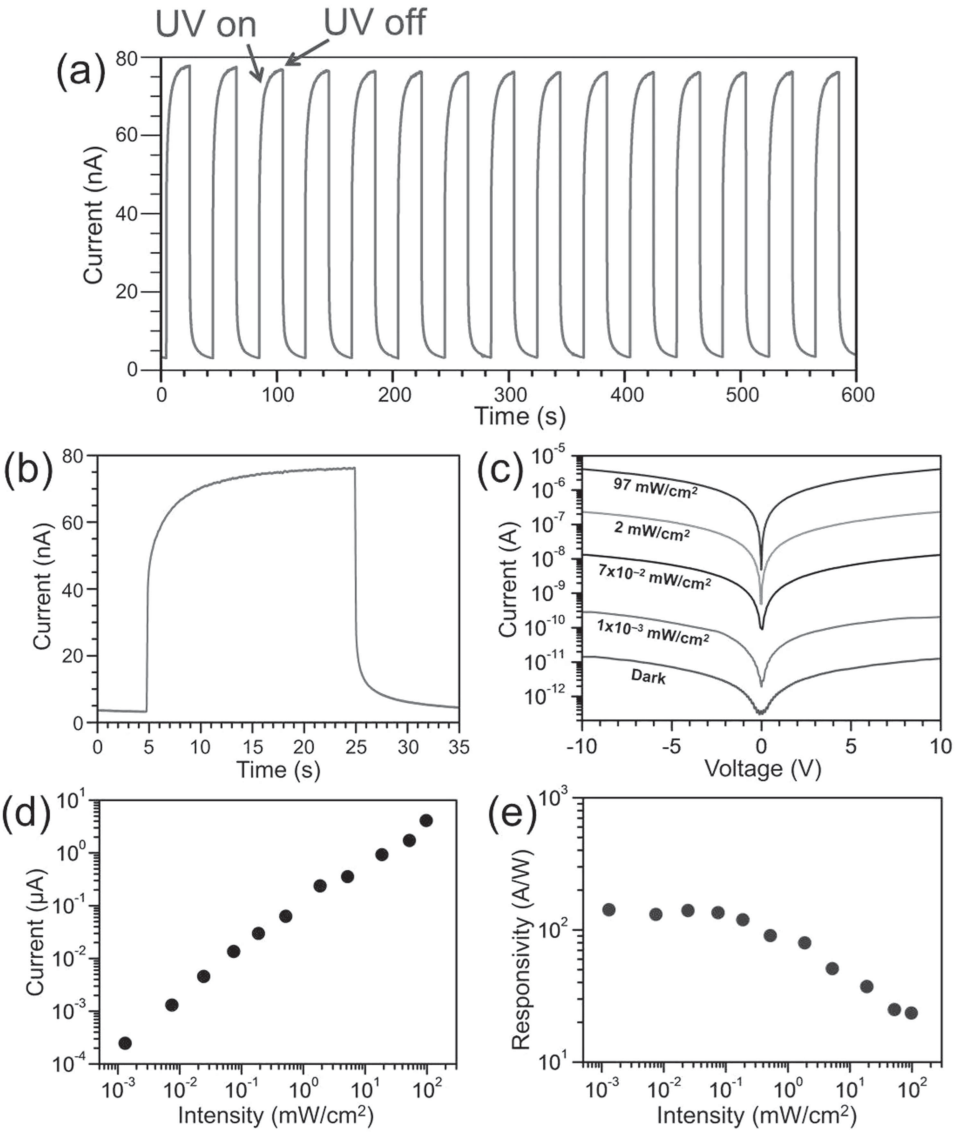

Figure 2. (a) Photoresponses of the built-in photodetector upon 70 μW cm^{-2} UV light illumination at a bias of 5 V. (b) Enlarged single cycle of the photoresponse in (a). (c) Typical *I–V* curves for the built-in photodetector measured at applied bias from −10 to 10 V in the dark and under UV light illumination with various power intensities. (d) Photocurrent and (e) Photoresponsivity of the built-in photodetector as a function of the incident UV light in a wide range from 1 μW cm^{-2} to 97 mW cm^{-2} at a bias of 10 V.

reaches 4 μA at a bias of 10 V when the power intensity of the UV light is varied to 97 mW cm^{-2}. However, the dark current is only 35 pA at a bias of 10 V, which is about five orders of magnitude smaller than the photocurrent. To show the selective detection of UV light, the photoresponse data of the built-in photodetector under visible light (wavelength: 412–569 nm) and near-infrared light (wavelength: >780 nm) irradiations were measured (Figure S3). From those results, we can observe the photoresponse of the built-in photodetector under visible light or near-infrared light irradiations is much smaller than that under UV light irradiation. Hence, it is supposed to ignore the effect from visible light or near-infrared light when measuring the UV light intensity. The dependence of photocurrent of the built-in photodetector on the incident light power density can be observed more obviously from Figure 2d. It is found that the photocurrent has a linear relationship with the incident light power density. No photocurrent saturation phenomenon occurs in the whole light intensity range. The responsivity of the photodetector is displayed in Figure 2e. This photodetector exhibits an excellent capacity to detect extremely weak optical signals. Even under an incident light power intensity of 1 μW cm^{-2}, the magnitude of photosensitivity has already approached two orders. Besides, the photoresponse data of deposited TiO_2 thin film was compared to that of 3D dendritic TiO_2 nanostructures. The results indicate the necessary of using 3D dendritic TiO_2 nanostructures (Figure S4) as the photodetector material.

The working mechanism of TENG is illustrated as **Figure 3**. For simplification, one of the glass substrate on the polymer

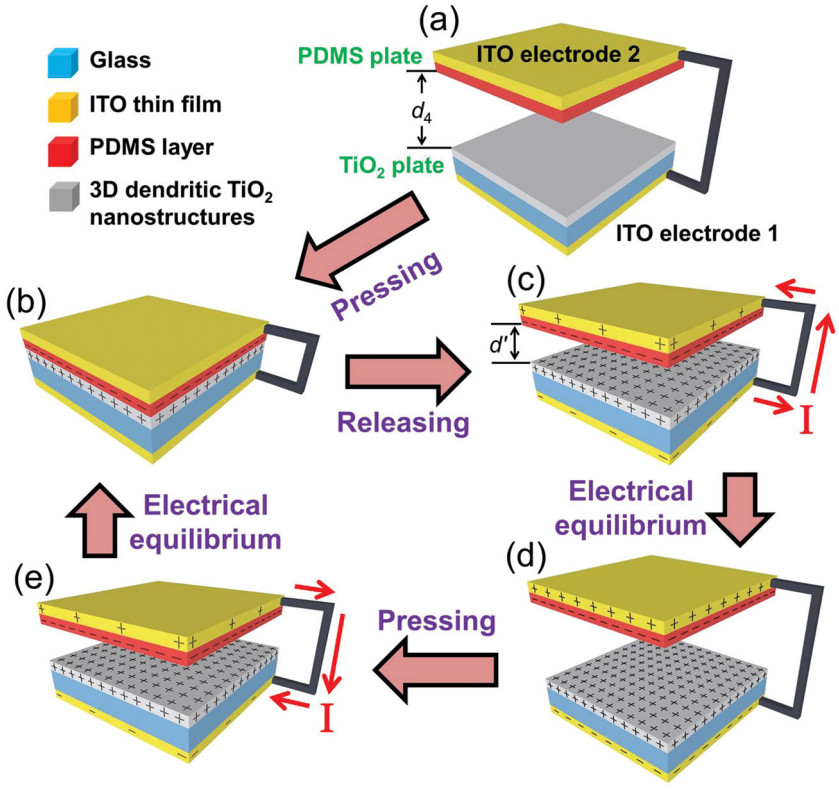

Figure 3. Working mechanism of the TENG. (a) Original status without any external force applied. (b) External force brings the two plates into contact, resulting in surface triboelectric charges. (c) Withdrawal of the force causes a separation and electrons flow from ITO electrode 2 through external load to the ITO electrode 1. (d) Charge distribution of TENG after the electrical equilibrium. (e) External force applied again make the electrons flow from ITO electrode 1 through external load to the ITO electrode 2.

plate is skipped in the drawing. At the original state (Figure 3a), there is no charge transfer happened before the contact of these two plates. When a force is applied to make PDMS plate and TiO_2 plate contact (Figure 3b), electrons will inject from TiO_2 into the PDMS, leaving positive charges on the TiO_2 surface.[17,33] As the force is withdrawn, the contact surfaces are separated, and an electric potential difference is then established between the two plates. If we define electric potential of the TiO_2 plate (U_{bottom}) as zero, electric potential of the PDMS plate (U_{top}) can be expressed by

$$U_{top} = \frac{\sigma d'}{\varepsilon_0}$$

where σ is the triboelectric charge density, ε_0 is the vacuum permittivity, and d' is the interlayer distance at a given state. Therefore, the open-circuit voltage (V_{oc}) will keep increasing until the PDMS plate fully reverts to the original position and reach the maximum value. For short-circuit case, the electrons will transfer from ITO electrode 2 to ITO electrode 1 because of the higher potential of TiO_2 plate than the PDMS plate (Figure 3c), thus contributing to the current. The inducted charge density (σ') in TENG can be calculated as

$$\sigma' = \frac{\sigma d' \varepsilon_1 \varepsilon_2 \varepsilon_3}{d_1 \varepsilon_2 \varepsilon_3 + d' \varepsilon_1 \varepsilon_2 \varepsilon_3 + d_2 \varepsilon_1 \varepsilon_3 + d_3 \varepsilon_1 \varepsilon_2}$$

where ε_1, ε_2, and ε_3 are the relative permittivity of PDMS, TiO_2, and glass, respectively, and d_1, d_2, and d_3 are the thickness of the PDMS layer, TiO_2 film, and glass substrate, respectively. Detailed derivation process is described in supporting information. Because d_1, d_2, d_3, ε_1, ε_2, and ε_3 are constants, and the triboelectric charge density is stable for a long time,[34] hence σ' can be determined by the gap distance d'. The change of d' will contribute to the redistribution of the charges between ITO electrode 1 and ITO electrode 2 through the external load, and finally reaches an equilibrium (Figure 3d). This is the first half cycle of the TENG operation. The maximum value of σ' is obtained by substituting the gap distance d_4 for d' in the above equation. Once the TENG is being pressed again, the electric potential difference starts to decrease as the two plates get closer to each other (Figure 3e). The V_{oc} will drop from the maximum value to zero when a full contact is made again between the plates. A reduction of the gap distance would make the PDMS plate a higher electric potential than the TiO_2 plate. Consequently, the electrons will flow from ITO electrode 1 to ITO electrode 2, until achieving a new equilibrium (Figure 3b), which is the second half cycle of TENG operation. This process corresponds to an instantaneous negative current.

A typical electrical output of TENG is shown in **Figure 4**. The TENG was mechanically triggered by a linear motor that provided dynamic impact with controlled force (28 N, Figure S5) at a frequency of 0.5 Hz. The V_{oc} and short-circuit current (I_{sc}) density were measured to characterize the performance of the TENG. From Figure 4a, when the ITO electrode of TiO_2 plate is connected to the positive probe of the electrometer, a positive voltage of 19 V is generated upon the release of the applied force. The voltage will hold at a plateau until next pressing deformation in the second half cycle. This is because in an open-circuit condition the electrons cannot flow to screen the potential difference between the two plates. The peak value of the I_{sc} reaches 0.8 μA (Figure 4b), corresponding to the first half cycle of operation. The integration of each current peak gives the total charges transferred in a half cycle of operation. The experimental data validate the working mechanism described in Figure 3. Then we measured the electrical output of the TENG with a reverse connection to the electrometer (Figure S6), and the generated V_{oc} and I_{sc} showed the corresponding opposite values in Figures 4a and b, indicating that the measured signals were generated by the TENG. The stability of the as-developed TENG is also tested. Figure S7 displays the output of TENG and SEM image of 3D dendritic TiO_2 nanostructures coated Glass after 2-hour operation. We can find the variation of output is less than 5% and the nanostructures maintain the originally dendrite-like morphology.

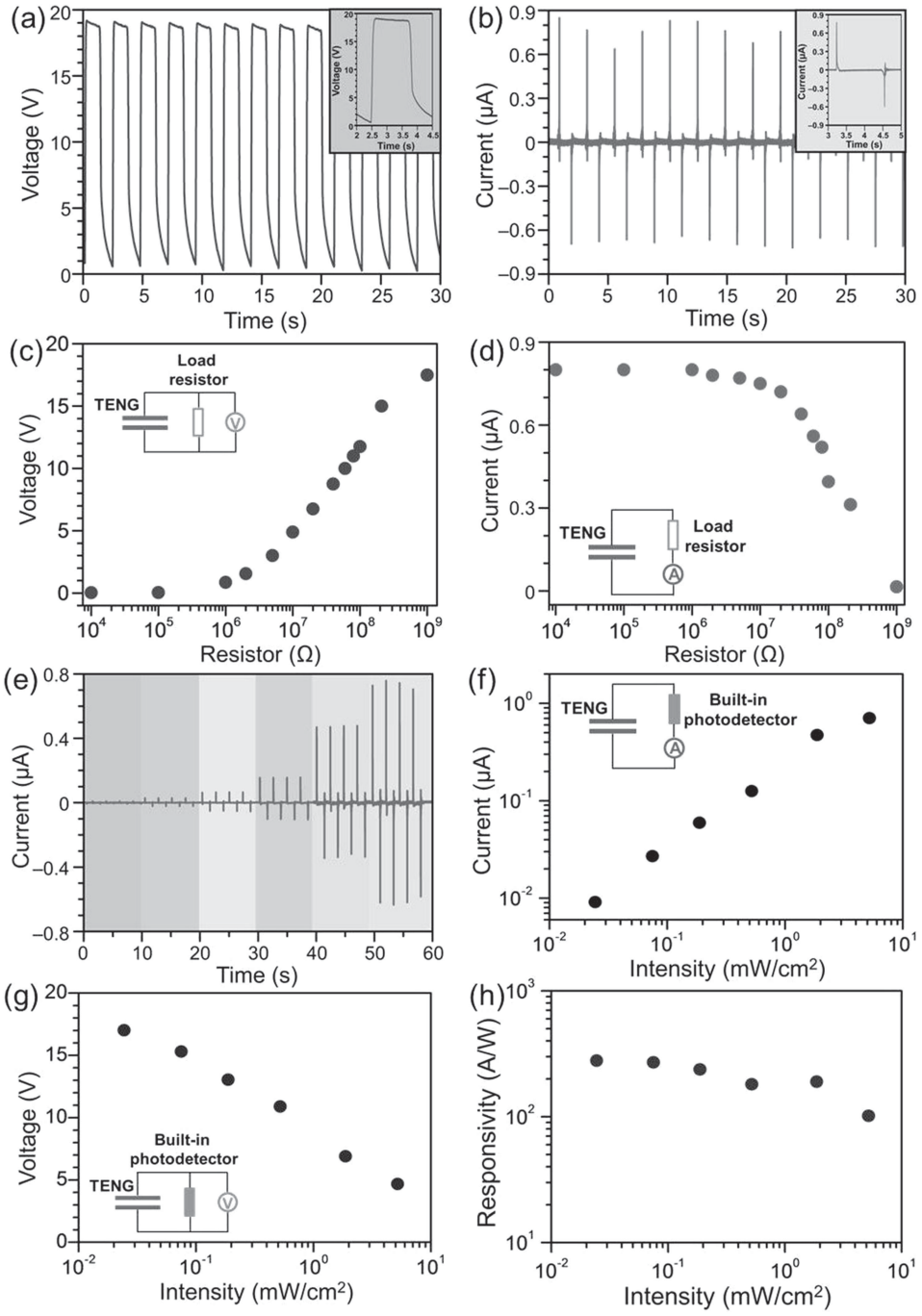

Figure 4. (a) Output voltage and (b) output current of the TENG. Insets of (a,b): enlarged view of one cycle. (c,d) The dependence of output voltage (c) and output current (d) of the TENG on the resistance of the external load. (e) Output current of the self-powered photodetector under UV light illumination with various power intensities. (f–h) The dependence of output current (f), output voltage (g), and responsivity (h) of the self-powered photodetector on UV light illumination with various power intensities.

Since the build-in photodetector functions as a variable external load resistor controlled by light intensity, we then measured the electrical output of TENG upon connecting directly to the external loads of different resistances. We can find that the output voltage across the load will generally increase with the increasing of resistor from 10 kΩ to 1 GΩ (Figure 4c), but the current across the load will follow an opposite trend (Figure 4d). The instantaneous power on the load will reach the maximum value of 0.22 W m^{-2} at a load resistance of 80 MΩ (Figure S8). As serially connecting the build-in photodetector to TENG, a new type of self-powered UV photodetector was demonstrated. Detailed circuit diagrams illustrating how the built-in photodetector connect to the measurement system are displayed in Figure S9. In the dark, the resistance of built-in photodetector

is larger, hence the output current will be lower and the output voltage will be higher and closed to the open circuit voltage of V_{oc}. While under UV light irradiation, the resistance of built-in photodetector drops, the output current of the self-powered photodetector when sensing UV light at different intensity is displayed in Figure 4e. The output current increases from 2 nA (in the dark) to 0.7 μA when the power intensity of incident UV light is varied to 7 mW cm^{-2}. The dependence of the output current on the incident light power density can be seen more clearly from Figure 4f. It is found that the output current has a linear relationship with the incident light power density from 20 μW cm^{-2} to 7 mW cm^{-2}.

Comparatively, the output voltage diminishes to 4.8 V when the power intensity of incident UV light is increased to 7 mW cm^{-2}. Although a linear relationship between the output voltage and incident light power intensity is also observed (Figure 4g), the change of the output current toward incident UV light with different intensities can reach up to 2 orders of magnitude and is more convenient to be used to determine the UV light intensity. The responsivity of the active UV photodetector is displayed in Figure 4h. This active UV photodetector exhibits an excellent capacity to detect the incident light intensity from 20 μW cm^{-2} to 7 mW cm^{-2}, which is more sensitive than the self-powered UV photodetector based on p-n junction. Finally we used PMMA and spring to assemble the self-powered UV photodetector and demonstrate as a portable device for UV light detection (**Figure 5**). Under periodic external mechanical deformation by biomechanical movements (finger tapping, 23 N), a linear relationship between the output current and power intensity of incident light similar to Figure 4f is observed. All of these reported results indicate that the as-developed active UV photodetector based on TENG shows great potential as a self-powered UV photodetector in the near future.

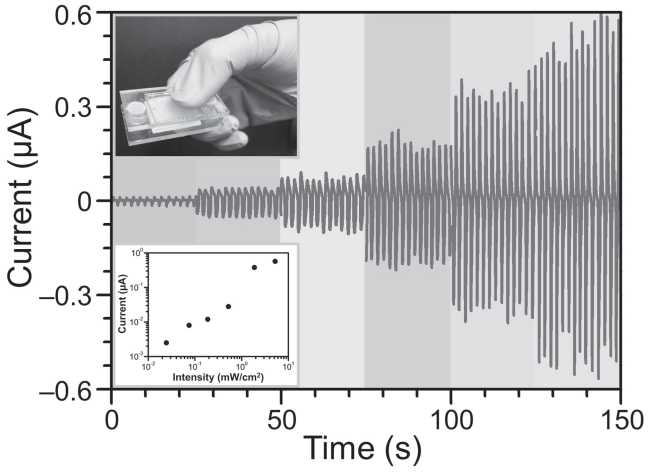

Figure 5. Output current of the stand-alone and self-powered UV photodetector triggered by biomechanical movements under UV light illumination with various power intensities. Insets are the photograph of the device and the dependence curve of output current on incident light intensity.

3. Conclusion

We have developed an integrated and active UV photodetector based on TENG configuration. Dendritic TiO_2 nanostructures were applied as the built-in photodetector and contact material of the TENG. The easy-fabricated, cost-effective, and robust TENG-based photodetector provides a rapid response time (rise time of 18 ms and decay time of 31 ms), an excellent responsivity reaching 280 A W^{-1}, and good linearity in a wide light intensity range from 20 μW cm^{-2} to 7 mW cm^{-2}. Through this work, we demonstrate the great potentials of TENG-based self-powered active sensors. We endeavor to lay the groundwork for related TENG studies and inspire the development of self-powered nanosensor toward other applications in the near future.

4. Experimental Section

Growth of 3D Dendritic TiO_2 Nanostructures on Glass Substrates: Pieces of glass (2.0 cm × 2.5 cm) ultrasonically cleaned in acetone, ethanol, and water for 30 min respectively, were then placed in separated 50 mL glass bottles filled with $TiCl_3$ solutions (0.1 M, 20 mL). The sealed glass bottles were heated in ovens at a temperature of 80 °C for 12 h, and then cooled in air. The growth cycles need to repeat at least 2 times to make sure the surface of glass was covered with 3D dendritic TiO_2 nanostructures. Finally the glass substrates were rinsed with water to remove the non-adsorbed TiO_2 nanomaterials and then annealed in an oven at 450 °C for 3 h.

TENG Fabrication: Thin films of Ni (300 nm) were deposited on the top of dendritic TiO_2 nanostructures by a RF magnetron sputtering deposition system as the built-in photodetector electrodes. ITO thin films (50 nm) were deposited on the back of 3D dendritic TiO_2 nanostructures coated glass substrate (TiO_2 plate) and on the other clean glass substrate (PDMS plate) through a DC magnetron sputtering deposition system. ITO thin film was selected as the contacting electrode due to its high transparency property. On the PDMS plate, fluid PDMS that consists of base and curing agent in a ratio of 5:1 was spin-coated on the ITO thin film and then cured at 110 °C for 60 min to form a 10 μm-thick layer. Finally, copper wires were connected to the Ni electrodes and ITO electrodes as leads for subsequent electrical measurements.

Characterization: A LEO 1530 field emission scanning electron microscope (SEM) was used to measure the size and shape of the 3D dendritic TiO_2 nanostructures. A PANalytical X'Pert PRO diffractometer with Cu Kα radiation (λ = 0.15418 nm) and a Nicolet Almega dispersive Raman spectrometer were used to measure the X-ray diffraction (XRD) pattern and Raman spectrum of the 3D dendritic TiO_2 nanostructures. The electrical outputs of the as-developed TENGs were measured using a programmable electrometer (Keithley Model 6514) and a low-noise current preamplifier (Stanford Research System Model SR570). A 300 W Xenon lamp equipped with a band pass filter (275–375 nm) was used as light source. The output power for the UV light source was measured using a Newport 1916C optical power meter. The external force was determined by a commercial force plate sensor (Vernier Model FP-BTA).

Supporting Information

Supporting Information is available from the Wiley Online Library or from the author.

Acknowledgements

Z.-H. Lin and G. Cheng contributed equally to this work. This work was supported by MURI, the US Department of Energy, Office of Basic

Energy Sciences (DE-FG02–07ER46394), NSF, NSFC (61176067), and the "thousands talents" program for pioneer researcher and his innovation team, China.

Received: August 12, 2013
Revised: October 27, 2013
Published online: January 21, 2014

[1] S. Xu, Y. Qin, C. Xu, Y. Wei, R. Yang, Z. L. Wang, *Nat. Nanotechnol.* **2010**, *5*, 366.
[2] Y. Yang, Z.-H. Lin, T. Hou, F. Zhang, Z. L. Wang, *Nano Res.* **2012**, *5*, 888.
[3] E. Katz, A. F. Bückmann, I. Willner, *J. Am. Chem. Soc.* **2001**, *123*, 10752.
[4] L. Deng, C. Chen, M. Zhou, S. Guo, E. Wang, S. Dong, *Anal. Chem.* **2010**, *82*, 4283.
[5] M. Lee, J. Bae, J. Lee, C.-S. Lee, S. Hong, Z. L. Wang, *Energy Environ. Sci.* **2011**, *4*, 3359.
[6] D. Wen, L. Deng, S. Guo, S. Dong, *Anal. Chem.* **2011**, *83*, 3968.
[7] Q. Yang, Y. Liu, Z. Li, Z. Yang, X. Wang, Z. L. Wang, *Angew. Chem. Int. Ed.* **2012**, *51*, 6443.
[8] B. Tian, X. Zheng, T. J. Kempa, Y. Fang, N. Yu, G. Yu, J. Huang, C. M. Lieber, *Nature* **2007**, *449*, 885.
[9] Z. L. Wang, *Adv. Mater.* **2012**, *24*, 280.
[10] I. F. Akyildiz, J. M. Jornet, *Nano Commun. Netw.* **2010**, *1*, 3.
[11] Z. L. Wang, *Sci. Am.* **2008**, *298*, 82.
[12] Z. L. Wang, J. Song, *Science* **2006**, *312*, 242.
[13] F.-R. Fan, Z.-Q. Tian, Z. L. Wang, *Nano Energy* **2012**, *1*, 328.
[14] G. Zhu, Z.-H. Lin, Q. Jing, P. Bai, C. Pan, Y. Yang, Y. Zhou, Z. L. Wang, *Nano Lett.* **2013**, *13*, 847.
[15] S. Wang, L. Lin, Z. L. Wang, *Nano Lett.* **2012**, *12*, 6339.
[16] Z.-H. Lin, G. Zhu, Y. S. Zhou, Y. Yang, P. Bai, J. Chen, Z. L. Wang, *Angew. Chem. Int. Ed.* **2013**, *52*, 5065.
[17] Z.-H. Lin, Y. Xie, Y. Yang, S. Wang, G. Zhu, Z. L. Wang, *ACS Nano* **2013**, DOI: 10.1021/nn401256w.
[18] D. Walker, M. Razeghi, *Opto-Electron. Rev.* **2000**, *8*, 25.
[19] E. Monroy, F. Omnès, F. Calle, *Semicond Sci. Technol.* **2003**, *18*, R33.
[20] B. Tian, C. M. Lieber, *Pure Appl. Chem.* **2011**, *83*, 2153.
[21] X. Li, C. Gao, H. Duan, B. Lu, X. Pan, E. Xie, *Nano Energy* **2012**, *1*, 640.
[22] X. Li, C. Gao, H. Duan, B. Lu, Y. Wang, L. Chen, Z. Zhang, X. Pan, E. Xie, *Small* **2013**, DOI: 10.1002/smll.201202408.
[23] Y.-Q. Bie, Z.-M. Liao, H.-Z. Zhang, G.-R. Li, Y. Ye, Y.-B. Zhou, J. Xu, Z.-X. Qin, L. Dai, D.-P. Yu, *Adv. Mater.* **2011**, *23*, 649.
[24] S. M. Hatch, J. Briscoe, S. Dunn, *Adv. Mater.* **2013**, *25*, 867.
[25] E. Hosono, S. Fujihara, K. Kakiuchi, H. Imai, *J. Am. Chem. Soc.* **2004**, *126*, 7790.
[26] S. Hoang, S. P. Berglund, R. R. Fullon, R. L. Minter, C. B. Mullins, *J. Mater. Chem. A* **2013**, *1*, 4307.
[27] J. Zhang, M. Li, Z. Feng, J. Chen, C. Li, *J. Phys. Chem. B* **2006**, *110*, 927.
[28] Z. Sun, J. H. Kim, Y. Zhao, F. Bijarbooneh, V. Malgras, Y. Lee, Y.-M. Kang, S. X. Dou, *J. Am. Chem. Soc.* **2011**, *133*, 19314.
[29] X. Wang, B. Liu, Q. Wang, W. Song, X. Hou, D. Chen, Y.-B. Cheng, G. Shen, *Adv. Mater.* **2013**, *25*, 1479.
[30] K. Q. Peng, S. T. Lee, *Adv. Mater.* **2011**, *23*, 198.
[31] D. Wu, Y. Jiang, Y. Zhang, Y. Yu, Z. Zhu, X. Lan, F. Li, C. Wu, L. Wang, L. Luo, *J. Mater. Chem.* **2012**, *22*, 23272.
[32] B. Nie, J.-G. Hu, L.-B. Luo, C. Xie, L.-H. Zeng, P. Lv, F.-Z. Li, J.-S. Jie, M. Feng, C.-Y. Wu, Y.-Q. Yu, S.-H. Yu, *Small* **2013**, DOI: 10.1002/smll.201203188).
[33] D. J. Lacks, R. M. Sankaran, *J. Phys. D: Appl. Phys.* **2011**, *44*, 453001.
[34] P. K. Watson, Z. Z. Yu, *J. Electrost.* **1997**, *40–41*, 67.